



PERGAMON

International Journal of Impact Engineering 25 (2001) 573–597

---

---

INTERNATIONAL  
JOURNAL OF  
**IMPACT  
ENGINEERING**

---

---

[www.elsevier.com/locate/ijimpeng](http://www.elsevier.com/locate/ijimpeng)

# Normal penetration of an eroding projectile into an elastic–plastic target

I.V. Roisman\*, A.L. Yarin, M.B. Rubin

*Faculty of Mechanical Engineering, Technion-Israel Institute of Technology, 32000 Haifa, Israel*

Received 17 December 1998; received in revised form 30 September 2000; accepted 3 November 2000

---

## Abstract

The main objective of the present work is to describe normal penetration of a deformable projectile into an elastic–plastic target. The force imposed on the projectile by the target is generally a complex function of the strength of the target material, the projectile velocity, its diameter and shape, as well as the instantaneous penetration depth. When this force exceeds a certain critical value the projectile begins to deform. At moderate-to-high values of the impact velocity, the projectile's tip material flows plastically with large deformations causing the formation of a mushroom-like configuration. This process is accompanied by erosion of the projectile material. In the rear (“elastic”) part of the projectile the deformations remain small and the region can be approximated as a rigid body being decelerated by the projectile's yield stress. The general model allows one to predict the penetration depth, the projectile's eroded length and the crater diameter. It has been shown that in the limit of very high impact velocities the present model reduces to the well-known form of the hydrodynamic theory of shaped-charge jets. Also, a simplified asymptotic formula for the crater radius has been derived which includes the effect of the target's yield stress and compares well with experimental data for very high impact velocities. © 2001 Elsevier Science Ltd. All rights reserved.

---

## 1. Introduction

A number of different models have been developed to analyze the penetration process which focus attention on different ranges of impact velocity. For relatively high impact velocities the projectile and target materials flow like fluids, with the influence of their yield strengths being

---

\* Corresponding author. Fachgebiet Strömungslehre und Aerodynamick, Technische Universität Darmstadt, Petersenstr. 30, D-64287 Darmstadt, Germany. Tel.: + 49-6151-163-893.

E-mail address: [roisman@sla.tu-darmstadt.de](mailto:roisman@sla.tu-darmstadt.de) (I.V. Roisman).

negligibly small compared to inertial effects. This allows one to develop a hydrodynamic theory of penetration of the type considered in [1–3]. In these works, both the target and projectile are modeled as inviscid fluids with purely inertial resistance to deformation. Alternative models, considered in [4–6], modify the Bernoulli equation by adding plastic terms proportional to the yield strengths of the target and projectile.

In the time-dependent model of [7], some assumptions are made concerning the velocity and stress profiles in the projectile and the target. The axial momentum equation is integrated along the projectile and target axes and the initial interfacial velocity is found from the shock jump conditions. This model also uses empirical data for the crater diameter as a function of the projectile's initial velocity.

Another method uses an integral work rate balance to predict penetration of a rigid or deformable/eroding projectile into a rigid-plastic target. In this method, the velocity field is assumed to take different functional forms in several different target domains and the work rate balance is used to determine various coefficients. This approach was exploited to predict penetration of a rigid blunt cylindrical projectile in [8] and deformable projectiles in [9,10].

The approach in [11–13] allows one to significantly improve the characterization of the velocity field in the target and projectile. Specifically, the velocity field is assumed to be an irrotational field that is derived from a velocity potential.

The main objective of the present work is to develop an approximate solution of the problem of normal penetration of a deformable projectile into a semi-infinite elastic–plastic target. Here, the approach developed in [14,15] for rigid projectiles is generalized to include projectile deformation and mass loss. Again, the model uses an irrotational velocity field which corresponds to the motion of an ovoid of Rankine penetrating an elastic–plastic target. The target region is subdivided into an elastic region ahead of the projectile and a rigid-plastic region near the projectile. The momentum equation is solved exactly (when the radius of the ovoid is constant) in both the elastic and the rigid-plastic regions to find expressions for the pressure and the stress fields. The effects of the free front surface of the target are modeled approximately, and the force applied to the projectile is calculated analytically. Moreover, the model can be generalized without difficulty to include the effects of the free rear surface of finite thickness targets along the lines discussed in [14,15].

At moderate-to-high impact velocities it is assumed that plastic flow takes place in the whole tip region of the projectile. This process is accompanied by erosion of projectile material (Projectile Erosion: Mode PE). Mode PE is kinetically impossible at smaller projectile velocities, which are not considered in the present work.

In the following, expressions are developed for the pressure and the stresses in the target and projectile regions for Mode PE. Then, the balance of linear momentum in the target region, and in the deformed and rigid regions of the projectile, as well as at the plastic wave front are considered. The boundary conditions associated with the free front surface of the target, the free surface in the crater region that develops near the projectile, the target/projectile interface and the plastic wave front are satisfied approximately.

This paper is organized as follows. Section 2 describes the formulation of the model and Section 3 describes the projectile erosion mode (Mode PE). Section 4 presents the initial conditions and Section 5 discusses the solution procedure and comparison of the theoretical predictions with experimental data. Finally, Section 6 presents conclusions.

## 2. Description of the model

### 2.1. Basic assumptions

The target material is assumed to have a constant density  $\rho_T$ , the projectile material is assumed to have a constant density  $\rho_P$  and both remain incompressible. This means that the conservation of mass and the balance equation of linear momentum have the forms

$$\nabla \cdot \mathbf{v} = 0, \quad (2.1a)$$

$$\rho \dot{\mathbf{v}} = -\nabla p + \text{div } \boldsymbol{\sigma}', \quad (2.1b)$$

where the gradient operator  $\nabla$  and the divergence operator  $\text{div}$  are defined with respect to the current position of a material point, and  $\mathbf{v}$  is the absolute velocity of a material point. The Cauchy stress  $\boldsymbol{\sigma}$  has been separated into a pressure  $p$  and its deviatoric part  $\boldsymbol{\sigma}'$ , such that

$$\boldsymbol{\sigma} = -p\mathbf{I} + \boldsymbol{\sigma}', \quad (2.2a)$$

$$\boldsymbol{\sigma}' \cdot \mathbf{I} = 0, \quad (2.2b)$$

where  $\mathbf{I}$  is the unit tensor and  $\mathbf{A} \cdot \mathbf{B} = \text{tr}(\mathbf{A}^T \mathbf{B})$  denotes the scalar product between two tensors  $\mathbf{A}$  and  $\mathbf{B}$ .

At the instant when the projectile touches the target's front surface, the target material begins to deform elastically. However, at some point during the penetration process the target material begins to deform plastically and an elastic–plastic boundary propagates away from the projectile's tip. In the elastic region the strains remain small, whereas in the plastic region the strains can be very large. Furthermore, for simplicity it is assumed that the material response in the plastic regions is rate-insensitive and rigid-plastic so that the deviatoric stress can be approximated by

$$\boldsymbol{\sigma}' = \left(\frac{2}{3}\right)^{1/2} \frac{Y}{(\mathbf{D} \cdot \mathbf{D})^{1/2}} \mathbf{D}, \quad (2.3)$$

where  $Y$  is the constant yield stress in uniaxial tension (with  $Y = Y_P$  for the projectile and  $Y = Y_T$  for the target) and  $\mathbf{D}$  is the symmetric part of the velocity gradient. Also, in the elastic region of the target it is assumed that the material response is linear elastic and isotropic so that for isochoric motion the deviatoric stress is related to the linear strain tensor  $\boldsymbol{\varepsilon}$  by

$$\boldsymbol{\sigma}' = 2\mu\boldsymbol{\varepsilon}, \quad (2.4)$$

where  $\mu$  is the constant shear modulus.

### 2.2. Velocity field in the target and the shape of the target/projectile interface

Consider a cylindrical coordinate system with coordinates  $\{r, \theta, z\}$ , base vectors  $\{\mathbf{e}_r, \mathbf{e}_\theta, \mathbf{e}_z\}$ , and a fixed origin at the initial location of the front free surface of the target. The tip S of the eroding mushroom-like part of the projectile is located at  $z = x(t)$ .

It is convenient to divide the target and the projectile into four regions separated by the boundaries (see Fig. 1)  $z = z_1 \rightarrow -\infty$  associated with the target's rear surface;  $z_2$  associated with the elastic–plastic boundary in the target;  $z_3$  associated with the point S at the projectile's tip;

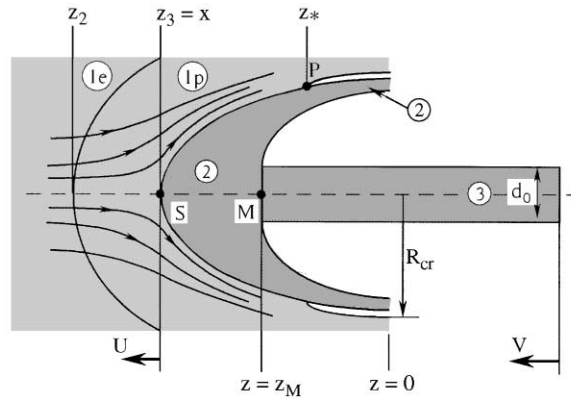


Fig. 1. Definition of different regions in the target and the projectile. (1e) elastic region in the target; (1p) plastic region in the target; (2) plastic region in the projectile; (3) rigid region in the projectile. An ovoid of Rankine is proposed as a good approximation of the interface between regions (1p) and (2).

$z_*$  associated with the separation point of the target material from the projectile material; and  $z_M$  associated with the rigid-plastic boundary in the projectile.

Point S with coordinates ( $z_3 = x, r = 0$ ) shown in Fig. 1 moves with velocity  $U$  so that the location of the projectile's tip is determined by the equation

$$\dot{x} = -U. \quad (2.5)$$

Moreover, since the projectile's tip deforms, the velocity  $U$  is smaller in magnitude than the velocity  $V$  of the projectile's rear part (region 3 in Fig. 1). The shape of the interface between the projectile and target material is approximated by an ovoid of Rankine with a variable radius  $R_\infty$  at infinity. This form is associated with a combination of the potentials of a single source and a uniform flow. It can be shown that this surface which is defined by  $r = R$  can be expressed in the parametric forms [14–17]

$$\xi = \Xi(R) = \frac{2R^2 - R_\infty^2}{2(R_\infty^2 - R^2)^{1/2}}, \quad (2.6a)$$

$$r = R(\xi) = \left[ \frac{R_\infty^2 - \xi^2}{2} + \frac{\xi}{2}(\xi^2 + 2R_\infty^2)^{1/2} \right]^{1/2}, \quad (2.6b)$$

$$\xi = z - x - \frac{R_\infty}{2}, \quad (2.6c)$$

where  $\xi$  is a coordinate measured relative to the source.

The flow field in the target (in regions 1e and p in Fig. 1) about the ovoid of Rankine is characterized by the velocity potentials

$$\phi_T^{\text{rel}} = UR_\infty \bar{\phi}^{\text{rel}}, \quad (2.7a)$$

$$\bar{\phi}^{\text{rel}} = \bar{\xi} - \frac{1}{4(\bar{\xi}^2 + \bar{r}^2)^{1/2}}, \quad (2.7b)$$

where the non-dimensional axial and radial coordinates  $\bar{\xi}$  and  $\bar{r}$  are defined by

$$\bar{\xi} = \frac{\xi}{R_\infty}, \quad (2.8a)$$

$$\bar{r} = \frac{r}{R_\infty}, \quad (2.8b)$$

$\phi_T^{\text{rel}}$  is the potential of the velocity field (relative to the system of coordinates associated with the interface surface) satisfying the continuity equation. The condition of impenetrability at the interface is satisfied exactly when  $R_\infty$  remains constant but only approximately when  $R_\infty$  varying with time. In this regard, it is noted that the length of the crater observed in a ballistic experiment usually significantly exceeds the change of the projectile diameter. Moreover, these craters are nearly cylindrical in shape. Therefore, the rate of change of  $R_\infty$  with time is neglected in determining the velocity and stress fields and the velocity field (2.7) is considered as quasi-stationary relative to the time derivative of  $R_\infty$ .

The above potential (2.7) relative to a point at rest in the target can be written as

$$\phi_T = -U\xi + \phi_T^{\text{rel}} = -\frac{UR_\infty}{4(\bar{\xi}^2 + \bar{r}^2)^{1/2}} \quad (2.9)$$

and the corresponding radial  $v_{rT}$  and axial  $v_{zT}$  components of the absolute velocity field in the target are given by

$$v_{rT} = UR_\infty^2 \left[ \frac{r}{4(\xi^2 + r^2)^{3/2}} \right], \quad (2.10a)$$

$$v_{zT} = UR_\infty^2 \left[ \frac{\xi}{4(\xi^2 + r^2)^{3/2}} \right] \quad (2.10b)$$

in both the elastic and plastic regions.

The main part of the velocity field used in the present work is associated with a source term which introduces a spherical component to the flow in the target due to a source that moves with the penetrating projectile. The justification for such a component follows from geometrical considerations related to impenetrability of the projectile surface. As was shown in [14,15], the velocity field (2.10) satisfies impenetrability of the projectile exactly if the projectile has the shape of an ovoid of Rankine and  $R_\infty$  is constant. An analytical approximation of the velocity field possessing a spherical component has also been introduced in [7] based on the results of numerous numerical simulations of the penetration process. Therefore, the kinematics in the target assumed in [7] is quite similar to that of [14,15] and the present work. In particular, the velocity component  $v_{zT}$  is proportional to  $\xi^{-2}$  ahead of the projectile in the present work as well as in [7,14,15].

### 2.3. Stress field in the target

Details of the analysis in the target can be found in the previous works [14,15]. In particular, using the velocity field (2.10) it can be shown that the rate of deformation tensor  $\mathbf{D}_T$  in the

target becomes

$$\mathbf{D}_T = \frac{UR_\infty^2}{4(\xi^2 + r^2)^{5/2}} \left[ (\xi^2 - 2r^2)\mathbf{e}_r \otimes \mathbf{e}_r + (\xi^2 + r^2)\mathbf{e}_\theta \otimes \mathbf{e}_\theta + (r^2 - 2\xi^2)\mathbf{e}_z \otimes \mathbf{e}_z - 3r\xi(\mathbf{e}_r \otimes \mathbf{e}_z + \mathbf{e}_z \otimes \mathbf{e}_r) \right]. \quad (2.11)$$

Thus, due to (2.3), the deviatoric stress  $\boldsymbol{\sigma}'_T$  in the target's plastic region, corresponding to the velocity field (2.10), can be written in the form

$$\boldsymbol{\sigma}'_T = Y_T \bar{\boldsymbol{\sigma}}', \quad (2.12a)$$

$$\bar{\boldsymbol{\sigma}}' = \frac{1}{3(\xi^2 + r^2)} \left[ (\xi^2 - 2r^2)\mathbf{e}_r \otimes \mathbf{e}_r + (\xi^2 + r^2)\mathbf{e}_\theta \otimes \mathbf{e}_\theta + (r^2 - 2\xi^2)\mathbf{e}_z \otimes \mathbf{e}_z - 3r\xi(\mathbf{e}_r \otimes \mathbf{e}_z + \mathbf{e}_z \otimes \mathbf{e}_r) \right]. \quad (2.12b)$$

Furthermore, using (2.12) it can be shown that

$$\text{div } \bar{\boldsymbol{\sigma}}' = \mathbf{V} \left[ -\ln \left( \frac{\xi^2 + r^2}{R_\infty^2} \right) \right]. \quad (2.13)$$

This result indicates that the balance of momentum equation can be solved exactly in the plastic zone of the target to obtain an expression for the pressure  $p_T$  in the target of the form

$$p_T = f_T(t) - \rho_T U^2 \left[ \frac{R_\infty^2 \xi}{4(\xi^2 + r^2)^{3/2}} + \frac{R_\infty^4}{32(\xi^2 + r^2)^2} \right] + \rho_T \dot{U} R_\infty \left[ \frac{R_\infty}{4(\xi^2 + r^2)^{1/2}} \right] - Y_T \ln \left\{ \frac{\xi^2 + r^2}{R_\infty^2} \right\}, \quad (2.14)$$

where the function  $f_T(t)$  depends on time only and has been determined in [14,15] by a matching condition at the elastic–plastic boundary in the target. For the case of a semi-infinite target this function can be written in the form

$$f_T(t) = Y_T \ln \bar{\xi}_2^2. \quad (2.15)$$

Also, in (2.14) the time rate of change of  $R_\infty$  has been neglected.

Due to the similarity of the velocity fields in [7,14,15] and in the present work, the pressure  $p_T$  predicted by (2.14) and (2.15) near the projectile's tip is quite close to the one predicted by Eqs. (8), (26), (43) in [7] (where some additional assumptions were made).

In Eq. (2.15),  $\bar{\xi}_2$  is the coordinate of the intersection of the elastic–plastic boundary with the projectile axis. This elastic–plastic boundary is determined by the values of  $r$  and  $\xi$  which cause the solution in the elastic region to satisfy the von Mises yield condition. In particular, the value of  $\bar{\xi}_2$  associated with the intersection of the elastic–plastic boundary with the axis  $r = 0$  can be determined analytically as a function of  $x$  by solving a quartic equation of the form (the detailed

derivation of this equation and the solution in the elastic region can be found in [15])

$$\tilde{\xi}_2^4 + 2\tilde{x}\tilde{\xi}_2^3 + \tilde{x}^2\tilde{\xi}_2^2 - 2\tilde{x}\tilde{\xi}_2 - \tilde{x}^2 = 0, \quad (2.16a)$$

$$\tilde{\xi}_2 = \left\{ \frac{4Y_T}{3\mu_T} \right\}^{1/2} \bar{\xi}_2, \quad (2.16b)$$

$$\tilde{x} = \left\{ \frac{4Y_T}{3\mu_T} \right\}^{1/2} \bar{x}, \quad (2.16c)$$

$$\bar{x} = \frac{x}{R_\infty}. \quad (2.16d)$$

Using expressions (2.12) and (2.14), the stress at the target/projectile interface can be expressed in terms of the vectors  $\{\mathbf{n}, \mathbf{e}_\theta, \boldsymbol{\tau}\}$

$$\boldsymbol{\sigma}_T = \sigma_{nnT} \mathbf{n} \otimes \mathbf{n} + \sigma_{\theta\theta T} \mathbf{e}_\theta \otimes \mathbf{e}_\theta + \sigma_{\tau\tau T} \boldsymbol{\tau} \otimes \boldsymbol{\tau} + \sigma_{n\tau T} (\mathbf{n} \otimes \boldsymbol{\tau} + \boldsymbol{\tau} \otimes \mathbf{n}), \quad (2.17a)$$

$$\sigma_{nnT} = -p_T + Y_T \left[ \frac{(-8 + 9\bar{R}^2)}{3(4 - 3\bar{R}^2)} \right], \quad (2.17b)$$

$$\sigma_{\theta\theta T} = -p_T + \frac{Y_T}{3}, \quad (2.17c)$$

$$\sigma_{\tau\tau T} = -p_T + Y_T \left[ \frac{(4 - 6\bar{R}^2)}{3(4 - 3\bar{R}^2)} \right], \quad (2.17d)$$

$$\sigma_{n\tau T} = Y_T \left[ \frac{-2\bar{R}(1 - \bar{R}^2)^{1/2}}{(4 - 3\bar{R}^2)} \right], \quad (2.17e)$$

$$p_T = f_T(t) + \rho_T U^2 \left[ \frac{(1 - 3\bar{R}^2)(1 - \bar{R}^2)}{2} \right] + \rho_T \dot{U} R_\infty \left[ \frac{(1 - \bar{R}^2)^{1/2}}{2} \right] + Y_T \ln[4(1 - \bar{R}^2)], \quad (2.17f)$$

where  $\mathbf{n}$  and  $\boldsymbol{\tau}$  are the outward unit normal and unit tangent to the interface and  $\mathbf{e}_\theta$  is the circumferential unit vector normal to  $\mathbf{n}$  and  $\boldsymbol{\tau}$ .

Note, that accounting for the effect of  $\dot{R}_\infty$  on the time derivative of the potential  $\phi_T$  leads to the following additional term  $\Delta p$  in the expression for the pressure at the target/projectile interface:

$$\Delta p = U \dot{R}_\infty Q(\bar{R}), \quad Q(\bar{R}) = (1 - \bar{R}^2)^{1/2} - \frac{2\bar{R}^4 - 3\bar{R}^2 + 1}{2}. \quad (2.18)$$

However, the rate of change of the projectile radius  $\dot{R}_\infty$  does not affect the velocity field defined by (2.9) directly. In particular, as  $\bar{R} \rightarrow 1$  the radial velocity does not approach  $\dot{R}_\infty$  as would be expected for cylindrical cavity expansion. This means, when  $\dot{R}_\infty \neq 0$  then the velocity field does not satisfy the condition of impenetrability of the target and projectile interfaces. In spite of this physical deficiency, the effect of  $\dot{R}_\infty$  is assumed to be small so term (2.18) is neglected even though  $R_\infty$  will be allowed to vary with time.

In view of the discussion in [14,15], the effect of  $\sigma_{nt}$  is neglected on the value of the axial force applied to the target/projectile interface. Thus, the force is given by

$$F = -2\pi R_\infty^2 \int_0^{\bar{R}_*} \sigma_{nn}(\bar{R}) \bar{R} d\bar{R}, \quad (2.19a)$$

$$\bar{R}_* = \frac{R_*}{R_\infty}, \quad (2.19b)$$

where  $\bar{R}_*$  is the radius of the separation point at the target/projectile interface which is determined by the condition that the normal stress  $\sigma_{nn}$  vanishes at this interface. For the case of a semi-infinite target, the drag force  $F = F_T$  applied by the target is given by (2.19) and can be expressed as [14,15]

$$F_T = \pi R_\infty^2 [A_T \dot{U} R_\infty + B_T U^2 + C_T] + \pi R_\infty^2 \bar{R}_*^2 f_T(t), \quad (2.20a)$$

$$A_T = \frac{1}{3} \rho_T [1 - (1 - \bar{R}_*^2)^{3/2}], \quad (2.20b)$$

$$B_T = \frac{1}{2} \rho_T \bar{R}_*^2 (1 - \bar{R}_*^2)^2, \quad (2.20c)$$

$$C_T = Y_T \left[ \bar{R}_*^2 \ln 4 - (1 - \bar{R}_*^2) \ln(1 - \bar{R}_*^2) - \frac{4}{9} \ln \left\{ \frac{4}{4 - 3\bar{R}_*^2} \right\} \right]. \quad (2.20d)$$

### 3. Derivation of the equations for projectile erosion during normal penetration

At moderate to high impact velocities the penetrating projectile flows plastically in the whole tip region whereas its rear part remains nearly undeformed. This process is accompanied by mass loss of the projectile material near its tip. In the present model of penetration of an eroding projectile, the target/projectile interface is approximated by an ovoid of Rankine of radius  $R_\infty$  (see Fig. 1). An irrotational velocity field in the projectile's deforming part is assumed which exactly satisfies the impenetrability condition for the target/projectile interface when  $R_\infty$  remains constant. However, this velocity field does not satisfy the impenetrability condition when  $R_\infty$  varies with time. In spite of this fact, it is expected that except for the very initial stages of penetration, the value of  $R_\infty$  does not change sharply (this is confirmed by the near cylindrical shapes of craters observed in experiments) so that the velocity field is used even when  $R_\infty$  changes. Furthermore, it is noted that at very high velocities, the region where the target and projectile materials are in contact (in the tip region of the projectile) represents only a small portion of the ovoid so its shape there is relatively unchanged by variations of  $R_\infty$ . Consequently, the rate of change of  $R_\infty$  is neglected in the present analysis of erosion even though  $R_\infty$  is allowed to vary with time.

Next, the balance of linear momentum in the deforming region of the projectile is solved exactly (for constant  $R_\infty$ ) to find expressions for the pressure and stress fields. The boundary conditions on the target/projectile interface and on the free lateral surface of the projectile are modeled approximately and the decelerations of the projectile's tip and of its rear part, as well as the radius of ovoid of Rankine are expressed analytically. A method for the estimation of the crater radius is also proposed.



### 3.1. Velocity field in the projectile and the equation of motion of its rigid tail

If the radius  $R_\infty$  of the ovoid is constant then the potential  $\phi_T^{\text{rel}}$  of the velocity field in the target [given by (2.7)] satisfies the continuity equation and the condition of impenetrability at the interface. It is clear that for any constant  $W$ , the velocity field with a potential relative to the projectile tip given in the form

$$\phi_P^{\text{rel}} = WR_\infty \bar{\phi}^{\text{rel}} \quad (3.1)$$

will also exactly satisfy the continuity equation and the condition of impenetrability at the interface (for  $R_\infty = \text{constant}$ ). Following the above-mentioned discussion, this potential is used to approximate the velocity field in the plastic zone of the projectile (region 2 in Fig. 1) near the target/projectile interface even when  $R_\infty$  varies with time. The value of  $W$  characterizes the rate of erosion of the projectile and will be found as a function of time.

Relative to a point at rest in the target, the above potential can be expressed as

$$\phi_P = -U\xi + \phi_P^{\text{rel}} = -\left[\frac{WR_\infty^2}{4(\xi^2 + r^2)^{1/2}} - (W - U)\xi\right]. \quad (3.2)$$

Eq. (3.2) yields the following expressions for the radial  $v_{rP}$  and axial  $v_{zP}$  components of the velocity field in the mushroom-like part of the projectile

$$v_{rP} = \frac{WR_\infty^2 r}{4(\xi^2 + r^2)^{3/2}}, \quad (3.3a)$$

$$v_{zP} = \left[\frac{WR_\infty^2 \xi}{4(\xi^2 + r^2)^{3/2}}\right] + W - U. \quad (3.3b)$$

This velocity field is not a good approximation of the real field in the outside region of the mushroom-like part of the projectile, since it corresponds to a source situated somewhere in the rigid portion of the projectile's tail. However, the velocity field (3.3) seems to be reasonably valid near the target/projectile interface.

In the present analysis, the projectile is separated into two regions. The mushroom-like tip region 2 has length  $\ell(t)$  (i.e. the distance between points S and M in Fig. 1), and the tail region 3 has length  $L(t)$  (i.e. the distance between point M and the free rear surface of the projectile in Fig. 1). It then follows that the current length  $(\ell + L)$  of the projectile is determined by the equation

$$\frac{d}{dt}(\ell + L) = -(V - U). \quad (3.4)$$

Moreover, the tail region 3 of the projectile is assumed to be a rigid body moving with uniform velocity  $V = V(t)$ . Consequently, since the yield stress  $Y_P$  acts on the tail at the surface M it follows from rigid body dynamics that

$$\dot{V} = -\frac{Y_P}{\rho_P L}. \quad (3.5)$$

### 3.2. Stress field in the plastic zone of the projectile

Using the velocity field (3.3) in the plastic region 2 of the projectile (see Fig. 1), it can be shown that the rate of deformation tensor  $\mathbf{D}_P$  in the projectile becomes

$$\mathbf{D}_P = K \mathbf{D}_T, \quad (3.6a)$$

$$K = \frac{W}{U}, \quad (3.6b)$$

where the expression for  $\mathbf{D}_T$  in the target is given by (2.11). Thus, the deviatoric stress  $\boldsymbol{\sigma}'_P$  in the plastic region of the projectile, corresponding to the velocity field (3.3), can be written in the form

$$\boldsymbol{\sigma}'_P = Y_P \bar{\boldsymbol{\sigma}}', \quad (3.7)$$

where the non-dimensional tensor  $\bar{\boldsymbol{\sigma}}'$  is defined by (2.12b).

Furthermore, using (2.13), the balance of linear momentum can be solved in the plastic region 2 (Fig. 1) of the projectile to obtain an expression for the pressure  $p_P$  in the projectile of the form

$$p_P = f_P(t) - \rho_P W^2 \left[ \frac{R_\infty^2 \xi}{4(\xi^2 + r^2)^{3/2}} + \frac{R_\infty^4}{32(\xi^2 + r^2)^2} \right] + \rho_P \dot{U} \xi - Y_P \ln \left\{ \frac{\xi^2 + r^2}{R_\infty^2} \right\}, \quad (3.8)$$

where  $\dot{W}$  has been neglected in spite of the fact that  $\dot{U}$  has been retained. The function  $f_P(t)$  is determined using a matching condition for the normal stress at the boundary between regions 2 and 3 in the projectile (Fig. 1). Now, with the help of (3.7) and (3.8), Eq. (2.2a) can be evaluated on the surface of the projectile to express the normal stress  $\sigma_{nn}$  there as

$$\sigma_{nnP} = -p_P + Y_P \left[ \frac{(-8 + 9\bar{R}^2)}{3(4 - 3\bar{R}^2)} \right], \quad (3.9a)$$

$$p_P = f_P(t) + \rho_P W^2 \left[ \frac{(1 - 3\bar{R}^2)(1 - \bar{R}^2)}{2} \right] + \rho_P \dot{U} R_\infty \left[ \frac{2\bar{R}^2 - 1}{2(1 - \bar{R}^2)^{1/2}} \right] + Y_P \ln [4(1 - \bar{R}^2)]. \quad (3.9b)$$

These Eqs. (3.9) are used to calculate the axial force applied by the projectile material on the target.

### 3.3. Matching conditions at the target/projectile interface

It is of interest to note that for the special case when  $Y_T = Y_P$ , the present model will cause the normal stress to be continuous pointwise on the interface between regions 1p and 2 (see Fig. 1). For the more general case when  $Y_T \neq Y_P$ , it is possible to approximate this exact boundary condition by a matching condition equating the normal stress  $\sigma_{nn}$  in the target with the normal stress  $\sigma_{nn}$  in region 2 of the projectile at point S ( $\bar{R} = 0$ ) on the axis. Thus, from Eqs. (2.17a) and (3.9a), (3.9b) it can be shown that

$$f_P(t) = f_T(t) + \left[ \frac{2}{3} + \ln 4 \right] (Y_T - Y_P) + \frac{\rho_T}{2} U^2 - \frac{\rho_P}{2} W^2 + \frac{\rho_T + \rho_P}{2} \dot{U} R_\infty. \quad (3.10)$$

Since  $f_T(t)$  is known from (2.15), Eq. (3.10) determines the function  $f_P(t)$ .

Furthermore, the matching conditions at the target/projectile interface are each satisfied in an integral sense. In particular, the axial force applied to the projectile by the target through this interface is given by (2.20). The stress distribution (3.9) at the projectile's surface is used to obtain an expression for the force ( $-F_P$ ) applied by the projectile on the target material

$$F_P = \pi R_\infty^2 [A_P \dot{U} R_\infty + B_P W^2 + C_P] + \pi R_\infty^2 \bar{R}_*^2 f_P(t), \quad (3.11a)$$

$$A_P = \frac{1}{3} \rho_P [1 - (1 - \bar{R}_*^2)^{3/2} (1 + 2\bar{R}_*^2)], \quad (3.11b)$$

$$B_P = \frac{1}{2} \rho_P \bar{R}_*^2 (1 - \bar{R}_*^2)^2, \quad (3.11c)$$

$$C_P = Y_P \left[ \bar{R}_*^2 \ln 4 - (1 - \bar{R}_*^2) \ln (1 - \bar{R}_*^2) - \frac{4}{9} \ln \left\{ \frac{4}{4 - 3\bar{R}_*^2} \right\} \right]. \quad (3.11d)$$

Moreover, since the force ( $-F_P$ ) applied by the projectile on the target should be equal in magnitude and opposite in sign to the force ( $F_T$ ) applied by the target on the projectile, it is possible to use (3.10) and equate expressions (2.20) and (3.11) to deduce that

$$\rho_P W^2 = \rho_T U^2 + (Y_T - Y_P) G_Y(\bar{R}_*) + 2\dot{U} R_\infty \left[ \frac{G_P(\bar{R}_*)}{\bar{R}_*^4 (2 - \bar{R}_*^2)} \right], \quad (3.12a)$$

$$G_P(\bar{R}_*) = \frac{\rho_P}{3} [1 - (1 - \bar{R}_*^2)^{1/2} (1 + 2\bar{R}_*^2)] - \frac{\rho_T}{3} [1 - (1 - \bar{R}_*^2)^{3/2}] + \frac{\rho_T + \rho_P}{2} \bar{R}_*^2, \quad (3.12b)$$

$$G_Y(\bar{R}_*) = \frac{2[(1 - \bar{R}_*^2) \ln(1 - \bar{R}_*^2) - \frac{4}{9} \ln \{1 - \frac{3}{4} \bar{R}_*^2\} + \frac{2}{3} \bar{R}_*^2]}{\bar{R}_*^4 (2 - \bar{R}_*^2)}. \quad (3.12c)$$

### 3.4. Matching conditions at the rigid/plastic boundary in the projectile

In order to determine the location  $\xi = \xi_M$  of the rigid/plastic boundary in the projectile (point M in Fig. 1), use is made of the fact that at this point  $v_z = -V$ . Thus, assuming that  $\xi_M < 0$ , Eq. (3.3b) yields

$$\left[ \frac{W \xi_M R_\infty^2}{4(\xi_M^2 + r^2)^{3/2}} + W - U \right] \Big|_{r=0} = -V, \quad (3.13)$$

so that

$$\bar{\xi}_M^2 = \frac{W}{4(V + W - U)}, \quad (3.14a)$$

$$\bar{\xi}_M = \frac{\xi_M}{R_\infty} < 0, \quad (3.14b)$$

$$\ell = \frac{R_\infty}{2} + \xi_M, \quad (3.14c)$$

where use has been made of the fact that the projectile's tip is located by  $\xi = -R_\infty/2$  [see (2.6a)]. The conditions that the rear portion of the projectile is in a state of uniaxial stress and that at the elastic–plastic boundary the material yields, cause the axial stress  $\sigma_{zz}$  to be set equal to  $(-Y_P)$  at point M ( $\bar{\xi} = \bar{\xi}_M, \bar{r} = 0$ ). This is essentially equivalent to assuming [5] that the projectile is decelerated by its material strength.

Moreover, the continuity of the axial stress  $\sigma_{zz}$  at point M can be expressed using (3.3), (3.6), and (3.8) by the equations

$$\dot{U} R_\infty Q_M = -Q_F, \quad (3.15a)$$

$$Q_M = \rho_P \left[ \frac{1}{2} + \bar{\xi}_M + \frac{\rho_T}{2\rho_P} \right], \quad (3.15b)$$

$$Q_F = \frac{\rho_T}{2} U^2 + f_T + \left[ \frac{2}{3} + \ln 4 \right] Y_T - \frac{\rho_P}{2} (V - U)^2 - [1 + \ln(4\bar{\xi}_M^2)] Y_P. \quad (3.15c)$$

Then, expressions (3.12a) and (3.15a) yield an equation which is used to determine the rate of erosion  $W$ :

$$\rho_P W^2 = \rho_T U^2 + (Y_T - Y_P) G_Y(\bar{R}_*) - \frac{2G_P(\bar{R}_*) Q_F}{\bar{R}_*^4 (2 - \bar{R}_*^2) Q_M}. \quad (3.16)$$

It is emphasized that the matching conditions (3.15) at the rigid/plastic boundary in the projectile determines an expression for  $\dot{U}$  in terms of  $W$  [through the value of  $\bar{\xi}_M$  in (3.14a)] for each instant of time. Therefore, after the rate of erosion  $W$  has been determined using (3.16) [which is essentially the condition of continuity of force at the projectile/target interface], the value of  $\dot{U}$  is obtained by (3.15a).

Note also that since  $W^2$  must remain non-negative, Mode PE will be physically possible only when the right-hand side of (3.16) remains non-negative. Consequently, when the right-hand side of (3.16) becomes zero Mode PE ceases to exist and the calculation is terminated with the current penetration depth being taken as the final penetration depth even though the current projectile velocity is not necessarily zero. Actually, it is necessary to model another mode of deformation of the projectile in order to proceed with the calculation from the time that Mode PE ceases to exist until the time that the projectile ceases to penetrate the target. However, this additional mode of deformation is not modeled here so the present analysis is valid only for moderate to high impact velocities where the duration of Mode PE dominates the penetration process.

### 3.5. Separation point

In order to determine the point at which the target material separates from the projectile's surface, it is convenient to first determine the radius  $\bar{R}_1$  corresponding to the point at which the normal stress  $\sigma_{nnT}$  in the target vanishes. From (2.17b) and (2.17f) it follows that  $\bar{R}_1$  is the root

of the equation

$$\begin{aligned}\sigma_{mT}(\bar{R}_1) = & -f_T(t) - \rho_T U^2 \left[ \frac{(1 - 3\bar{R}_1^2)(1 - \bar{R}_1^2)}{2} \right] - Y_T \ln[4(1 - \bar{R}_1^2)] \\ & + \frac{Q_F}{Q_M} \left[ \frac{(1 - \bar{R}_1^2)^{1/2}}{2} \right] + Y_T \left[ \frac{(-8 + 9\bar{R}_1^2)}{3(4 - 3\bar{R}_1^2)} \right] = 0,\end{aligned}\quad (3.17a)$$

$$\bar{R}_1 = \frac{R_1}{R_\infty}.\quad (3.17b)$$

Moreover, using (3.9) and (3.10) it is possible to calculate the radius  $\bar{R}_2$  at which the normal stress  $\sigma_{nP}$  in the projectile (see region 2 of Fig. 1 which is the plastic mushroom-like part of the projectile) vanishes. Thus,  $\bar{R}_2$  is the root of the equation

$$\begin{aligned}\frac{\rho_P}{2} \bar{R}_2^2 (4 - 3\bar{R}_2^2) W^2 - \frac{\rho_T}{2} U^2 - Y_T \left[ \frac{2}{3} + \ln 4 \right] + Y_P \left[ \frac{\bar{R}_2^2}{4 - 3\bar{R}_2^2} - \ln(1 - \bar{R}_2^2) \right] \\ + \frac{Q_F}{Q_M} \left[ \frac{\rho_P}{2} \left\{ \frac{2\bar{R}_2^2 - 1}{(1 - \bar{R}_2^2)^{1/2}} \right\} + \frac{\rho_T + \rho_P}{2} \right] - f_T(t) = 0,\end{aligned}\quad (3.18)$$

where  $f_T(t)$  is known from (2.15).

Also, the normalized radius  $\bar{R}_4$  of the target/projectile interface (in the form of an ovoid of Rankine) at the front surface of the target is determined using (2.6) by

$$\bar{R}_4 = \left[ \frac{1 - \bar{\xi}_4^2}{2} + \frac{\bar{\xi}_4(\bar{\xi}_4^2 + 2)^{1/2}}{2} \right]^{1/2},\quad (3.19a)$$

$$\bar{\xi}_4 = -\frac{x}{R_\infty} - \frac{1}{2}.\quad (3.19b)$$

Expressions (2.17) and (3.9) for the stresses at the target/projectile interface are valid only over the section from the projectile's tip (point S in Fig. 1) to the separation point (point P in Fig. 1). So the separation point is determined by the normalized radius  $\bar{R}_*$  defined by

$$\bar{R}_* = \text{Min}[\bar{R}_1, \bar{R}_2, \bar{R}_4],\quad (3.20)$$

where  $\bar{R}_1$ ,  $\bar{R}_2$  and  $\bar{R}_4$  are calculated from (3.17), (3.18) and (3.19), respectively.

### 3.6. Scale parameter of the ovoid of Rankine

Consider a control volume (i.e. the mushroom-like region 2 of the projectile) as a body of revolution with the generatrix SPP<sub>1</sub>M<sub>1</sub>M (Fig. 2). Here point S is the projectile tip and point P is the separation point. The median cross-section PP<sub>1</sub> of the sheet of material flowing out of the control volume is assumed to be sufficiently thin for the velocity profile there to be uniform. Also the stress is assumed to be uniform over the surface PP<sub>1</sub>. The surface M<sub>1</sub>P<sub>1</sub> is a free surface; and the velocity and stress profiles over the cross-section MM<sub>1</sub> are assumed to be uniform.

$$v_z^{\text{rel}}|_{\bar{R}=\bar{R}_*} = UK \left[ 1 + \frac{\bar{\xi}_*}{4(\bar{\xi}_*^2 + \bar{R}_*^2)^{3/2}} \right]. \quad (3.23c)$$

The value of  $\sigma_{\tau\tau}$  at the separation point (where  $\sigma_{nn} = 0$ ) can be evaluated using (2.2a), (2.6), (2.12) and (3.7) to obtain

$$\sigma_{\tau\tau} = Y_P \left[ \frac{(4 - 5\bar{R}_*^2)}{(4 - 3\bar{R}_*^2)} \right]. \quad (3.24)$$

Thus, the conservation of mass and the axial component of the balance of linear momentum for the given control volume can be written in the forms

$$A|_{PP_1} v^{\text{rel}}|_{\bar{R}=\bar{R}_*} - A|_{MM_1} (V - U) = 0, \quad (3.25a)$$

$$F_T = Y_P A|_{MM_1} - \sigma_{\tau\tau}|_{\bar{R}=\bar{R}_*} (\mathbf{e}_z \cdot \mathbf{e}_\tau) A|_{PP_1} + \rho_P A|_{MM_1} (V - U)^2 + \rho_P A|_{PP_1} \{v^{\text{rel}}|_{\bar{R}=\bar{R}_*}\}^2 (\mathbf{e}_z \cdot \mathbf{e}_\tau), \quad (3.25b)$$

where  $F_T$  is the axial force applied to the projectile by the target. Next, the impenetrability condition associated with the target/projectile interface

$$(\mathbf{e}_z \cdot \mathbf{e}_\tau)|_{\bar{R}=\bar{R}_*} = \left\{ \frac{v_z^{\text{rel}}}{v^{\text{rel}}} \right\} \Big|_{\bar{R}=\bar{R}_*} \quad (3.26)$$

and (3.21) are used, and (3.25a) is substituted into Eq. (3.25b) to obtain

$$F_T = Y_P \pi \frac{d_0^2}{4} - \left[ \sigma_{\tau\tau} \pi \frac{d_0^2}{4} \frac{(V - U)}{(v^{\text{rel}})^2} v_z^{\text{rel}} \right] \Big|_{\bar{R}=\bar{R}_*} + \rho_P \pi \frac{d_0^2}{4} (V - U)^2 + \rho_P \pi \frac{d_0^2}{4} (V - U) v_z^{\text{rel}}|_{\bar{R}=\bar{R}_*}. \quad (3.27)$$

Moreover, equating expressions (2.20a) and (3.27), and using result (3.15a), it is possible to obtain an expression for the radius  $R_\infty$  of the ovoid of Rankine that approximates the target/projectile interface

$$R_\infty = \frac{d_0}{2} \left[ \frac{(V - U) \{ \rho_P (V - U) + \rho_P v_z^{\text{rel}} - (\sigma_{\tau\tau}/(v^{\text{rel}})^2) v_z^{\text{rel}} \} + Y_P}{-A_T(Q_F/Q_M) + B_T U^2 + C_T + \bar{R}_*^2 f_T(t)} \right]^{1/2}. \quad (3.28)$$

### 3.7. Crater radius

The ovoid of Rankine of radius  $R_\infty$  approximates the target/projectile interface in the region from the projectile tip up to the separation point where the normal component of the stress tensor vanishes. However, this shape cannot be used for the prediction of the crater radius, because it does not satisfy the condition that the crater surface is stress free (see Fig. 3a).

Here, the shape of the crater is approximated by another ovoid of Rankine of radius  $R_{cr}$  which is moving with the same velocity  $U$  (Fig. 3b). Although it is not possible to satisfy the boundary conditions for surface tractions pointwise on the crater surface, it is possible to satisfy these conditions approximately in integral sense. This is done by requiring the axial drag force  $F_T$  applied by the target on the projectile's tip to equal the axial force  $F_{cr}$  applied by the target over the whole surface of the new ovoid which approximates the crater (with radius  $R_{cr}$ ). In particular,  $F_{cr}$  can be calculated by using  $\bar{R}_* = 1$  in (2.20) and neglecting the term associated with  $\dot{U}$  to obtain

$$F_{cr} = \pi R_{cr}^2 [f_T(t) + \frac{5}{9} Y_T \ln 4]. \quad (3.29)$$

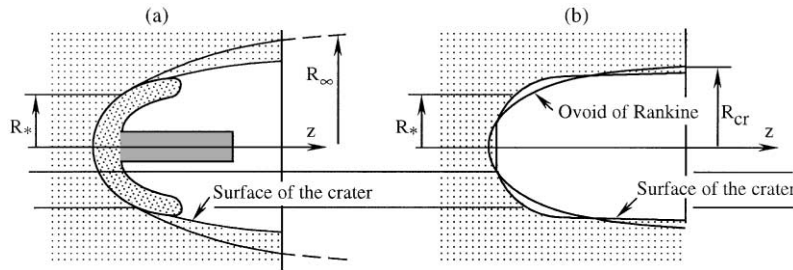


Fig. 3. Determination of the crater diameter.

Now, the expression for  $F_T$  is calculated by Eq. (2.20) where  $\bar{R}_*$  and  $R_\infty$  are determined using expressions (3.20) and (3.28). Thus, solving (3.29) for the crater radius  $R_{cr}$  and equating  $F_{cr}$  with  $F_T$  yields

$$R_{cr} = \left[ \frac{F_T}{\pi \{f_T(t) + \frac{5}{9} Y_T \ln 4\}} \right]^{1/2}. \quad (3.30)$$

### 3.8. Very high impact velocities

For the case of very high impact velocities, the pressure and the inertial effects dominate the effects of deviatoric stresses. Also, the penetration process can be modeled assuming nearly steady-state conditions with the deceleration of the projectile tip  $\dot{U}$  being neglected. Specifically,  $\{Y_T, Y_P, \dot{U}\}$  are neglected in Eq. (3.12a) to obtain

$$\frac{W}{U} = \alpha, \quad (3.31a)$$

$$\alpha = \left\{ \frac{\rho_T}{\rho_P} \right\}^{1/2}. \quad (3.31b)$$

Furthermore, for the case of penetration into a semi-infinite target,  $f_T(t) = 0$ , and  $Q_F, Y_T$  and  $Y_P$  are neglected in (3.15c) to deduce that

$$\rho_T U^2 = \rho_P (V - U)^2, \quad (3.32a)$$

$$U = \frac{V}{1 + \alpha}. \quad (3.32b)$$

Since Eq. (3.32a) is the same as that used in [1], this analysis shows that the present model asymptotically approaches the hydrodynamic treatment. Moreover, the more general model, which includes strength effects, will be shown to produce reasonably good agreement with experimental data for moderate impact velocities (between 1500 and 3000 m/s). Therefore, the general model produces the usual S-shaped curve for penetration depth vs impact velocity, with the importance of strength effects for moderate impact velocities being significant, as was recently discussed in [18].



Next, using the assumptions of this section, Eq. (3.17a) can be solved for the separation point at which the normal stress vanishes to deduce from (2.6a) that

$$\bar{R}_* = \bar{R}_1 = \frac{1}{\sqrt{3}}, \quad (3.33a)$$

$$\bar{\xi}_* = \left\{ \frac{\xi}{R_\infty} \right\} \bigg|_{R=\bar{R}_*} = -\frac{1}{2\sqrt{6}}. \quad (3.33b)$$

Now, since  $\dot{U}$  and  $Y_T$  are neglected and  $f_T(t) = 0$ , it follows from (2.20) that

$$B_T = \frac{2}{27}\rho_T, \quad (3.34a)$$

$$C_T = 0, \quad (3.34b)$$

$$F_T = \frac{2}{27}\pi R_\infty^2 \rho_T U^2. \quad (3.34c)$$

Moreover, Eqs. (3.6b) and (3.33) can be used to rewrite (3.23c) in the form

$$v_z^{\text{rel}}|_{R=\bar{R}_*} = \frac{7}{9}W. \quad (3.35)$$

Furthermore, it is noted that for the case when  $Y_P = 0$ , that the tangential stress  $\sigma_{\tau\tau}$  also vanishes at the separation point

$$\sigma_{\tau\tau} = 0, \quad (3.36)$$

so that substitution of (3.31), (3.32), (3.34)–(3.36) into (3.28) with  $Q_F = f_T = Y_P = 0$ , yields the following simple expression for the radius  $R_\infty$  of the ovoid of Rankine:

$$R_\infty = \sqrt{6}d_0. \quad (3.37)$$

At this point it is observed that if  $Y_T$  is set equal to zero in (3.30) with  $f_T = 0$ , then the resulting expression predicts the unphysical result that the crater radius  $R_{cr}$  approaches infinity at very high impact velocities. This result is consistent with the conclusion presented in [19] that the crater radius cannot be calculated within the framework of the theory based on the ideal fluid model. Indeed, such a model predicts that the crater can expand infinitely without plastic dissipation. Consequently, the plastic part of the total force  $F_{cr}$  applied to the projectile cannot be neglected, as compared with its inertial part, even at very high impact velocities [see Eq. (3.29)]. Thus, using (2.15) for  $f_T$ , (3.34c) for  $F_T$ , (3.37) for  $R_\infty$ , Eq. (3.30) yields an alternative expression for the crater radius  $R_{cr}$  of the form

$$R_{cr} = 2 \left[ \frac{\rho_T}{Y_T \{5 \ln 4 + 9 \ln(\bar{\xi}_2^2)\}} \right]^{1/2} d_0 U. \quad (3.38)$$

Next, using (3.32b), this expression for the crater radius can be rewritten in the form

$$R_{cr} = \frac{2d_0}{1 + \alpha} \left[ \frac{\rho_T V^2}{Y_T \{5 \ln 4 + 9 \ln(\bar{\xi}_2^2)\}} \right]^{1/2}, \quad (3.39)$$

which is used for very high impact velocities only.

### 3.9. Quasi-steady-state stage of penetration

For the case of long rod penetration, as noted in [20], the projectile motion is approximately steady state for a significant portion of the penetration process. Therefore, the terms corresponding to the projectile deceleration (which include the factor  $\dot{U}$ ) can be neglected during this portion of the process. Consequently, the differential equation (3.15) and Eq. (3.16) can be reduced to the following system of algebraic equations

$$\frac{\rho_T}{2}U^2 + f_T + \left[ \frac{2}{3} + \ln 4 \right] Y_T - \frac{\rho_P}{2}(V - U)^2 - [1 + \ln(4\bar{\xi}_M^2)] Y_P = 0, \quad (3.40a)$$

$$\rho_P W^2 = \rho_T U^2 + (Y_T - Y_P) G_Y(\bar{R}_*), \quad (3.40b)$$

where  $G_Y(\bar{R}_*)$  is defined in (3.12c), and  $\bar{\xi}_M$ , which depends on  $U$  and  $W$ , is defined in (3.14). Eqs. (3.40) have forms very similar to the modified Bernoulli equation proposed in [4–6]. In particular, note that for the small values of  $U$  the right-hand side of Eq. (3.40b) can be negative so the system will have no real solution. Physically, this determines the velocity at which Mode PE (projectile erosion) is kinetically inadmissible. Therefore, the calculation is terminated either when  $U$  vanishes and the penetration process stops or when the right-hand side of Eq. (3.40b) vanishes. Again, it is noted that if significant projectile velocity remains at this point then another mode of deformation is required to continue the calculation. This additional mode of deformation is not modeled and related cases with low impact velocities are not considered in the examples discussed later in this work.

## 4. Initial conditions

The initial stage of penetration is accompanied by the wave propagation in the target and projectile material. In order to account for this wave propagation process, the initial velocity of the target/projectile interface  $U_0$  is determined using the Rankine–Hugoniot jump conditions. To this end, denote  $u_{sP}$  and  $u_{sT}$  as the absolute shock velocities in the projectile and target, respectively. The material velocities in the target and in the projectile within the shocked region are equal to the velocity  $U_0$  of the target/projectile interface. Moreover, the relationship between the shock velocity and the material velocity in each of the materials is approximated by linear dependence as proposed in [7]

$$u_{sT} = c_{0T} + k_T U_0, \quad (4.1a)$$

$$V_0 - u_{sP} = c_{0P} + k_P (V_0 - U_0), \quad (4.1b)$$

where  $k_T, c_{0T}, k_P$  and  $c_{0P}$  are target and projectile material parameters and  $V_0$  is the impact velocity of the projectile. Values of these material parameters for some materials are given in Table 1.

Neglecting the deviatoric stresses in the shocked region, the pressures  $p_T$  and  $p_P$  at the target/projectile interface in the target and in the projectile, respectively, due to the

Table 1

A list of material constants for calculation of the Rankine–Hugoniot jump conditions [7]

Material	$c_0$ (m/s)	$k$
Aluminum (6061-T6)	5350	1.34
Armor steel	4500	1.49
Tungsten alloy	3850	1.44

jump conditions become

$$p_T = \rho_T u_{sT} U_0, \quad (4.2a)$$

$$p_P = \rho_P (V_0 - u_{sP})(V_0 - U_0). \quad (4.2b)$$

Thus, by equating  $p_T$  and  $p_P$  and using (4.1), it is possible to derive an expression for  $U_0$  of the form

$$U_0 = \frac{b - \sqrt{b^2 - 4ac}}{2a}, \quad (4.3a)$$

$$a = k_P - k_T \frac{\rho_T}{\rho_P}, \quad (4.3b)$$

$$b = 2k_P V_0 + c_{0P} + c_{0T} \frac{\rho_T}{\rho_P}, \quad (4.3c)$$

$$c = c_{0P} V_0 + k_P V_0^2, \quad (4.3d)$$

or

$$U_0 = \frac{c}{b} \quad \text{if } a = 0. \quad (4.4)$$

## 5. Solution of the equations of motion of the projectile

Using the above analysis, a computer program has been developed to numerically integrate the equations for the motion and deformation of a deformable projectile penetrating a target. Specifically, for the general case, the equations of motion (2.5), (3.4), (3.5), (3.15a) are integrated numerically, subject to the initial conditions

$$x(0) = 0, \quad L(0) = L_0 - \ell(0), \quad V = V_0, \quad U = U_0, \quad (5.1)$$

where use is been made of (2.15) for  $f_T$ ; (2.16) for  $\bar{\xi}_2$ ; (3.12b) for  $G_\rho$ ; (3.12c) for  $G_Y$ ; (3.14a) for  $\bar{\xi}_M$ ; (3.14c) for  $\ell$ ; (3.15b) for  $Q_M$ ; (3.15c) for  $Q_F$ ; (3.16) for  $W$ ; (3.20) for  $\bar{R}_*$ ; (3.17) for  $\bar{R}_1$ ; (3.18) for  $\bar{R}_2$ ; (3.19) for  $\bar{R}_4$ ; and (4.3) and (4.4) for  $U_0$ . Also, the crater radius  $R_{cr}$  is determined by (3.30). The calculation is terminated either when  $U$  or  $L$  vanishes, or when the right-hand side of (3.16) becomes negative and Mode PE ceases to be kinetically admissible. If  $U$  and/or  $V$  do not vanish at

Table 2

A list of experiments, references, and relevant material and geometrical properties

	Page in Ref. [21]	Projectile				Target	
		$d_0$ (mm)	$L_0/d_0$	$\rho_P$ (kg/m <sup>3</sup> )	$Y_P$ (MPa)	$\rho_T$ (kg/m <sup>3</sup> )	$Y_T$ (MPa)
EXP1	A78	5.4	10	7850	760	7850	990
EXP2	A76	2.5	10	7850	760	7850	990
EXP3	A74	5.4	10	7850	760	7850	430
EXP4	A75	5.4	10	7850	760	7850	590
EXP5	A104	5.8	10	15,500	820	7850	850
EXP6	A105	5.8	10	17,300	950	7850	850
EXP7	A106	5.8	10	17,000	1015	7850	850
EXP8	A206	6.35	7.5	7850	1263	7850	1263
EXP9	A200	6.35	7.5	7850	1263	7850	1448

the termination of the calculation then an additional mode of deformation is needed to complete the penetration process. However, such a mode is not modeled here. Consequently, the present model is valid for intermediate to high values of the impact velocity  $V_0$  where Mode PE dominates the penetration process. Also, it is noted that for low values of  $V_0$ , the projectile can be modeled as a rigid body [14,15].

### 5.1. Results of numerical simulations: comparison with experimental data and discussion

In order to examine the accuracy of the numerical solution of this model of penetration, the results of a number of computations have been compared with experiments chosen from the numerous data collected in [21]. A list of these experiments, together with the associated references and the relevant material and geometric properties is recorded in Table 2. Moreover, here attention is confined only to those cases where Mode PE dominates the penetration process. This excludes the range of impact velocity below about  $V_0 = 1500$  m/s as well as cases when the yield stress and the density of the projectile significantly exceed the corresponding parameters of the target. For these material parameters and range of impact velocities, Mode PE with erosion is not applicable and the projectile deforms without erosion or remains relatively rigid. This mode of deformation without erosion has not been modeled in the present work and remains a topic for future research.

Figs. 4–7 compare the numerical predictions of the penetration depth  $P$  with the experimental values. Fig. 4 shows the effect of varying the initial diameter  $d_0$  of the projectile, Fig. 5 shows the effect of varying the yield stress of the target material, Fig. 6 shows the effect of varying the material properties of the projectile, and Fig. 7 shows the effect of varying the yield stress of the target material. The agreement between the theoretical predictions (solid lines) and experimental data (symbols) is good.

At this point it should be emphasized that only the published values of the material properties have been used in these calculations and no attempt has been made to adjust material parameters to match the experimental data.

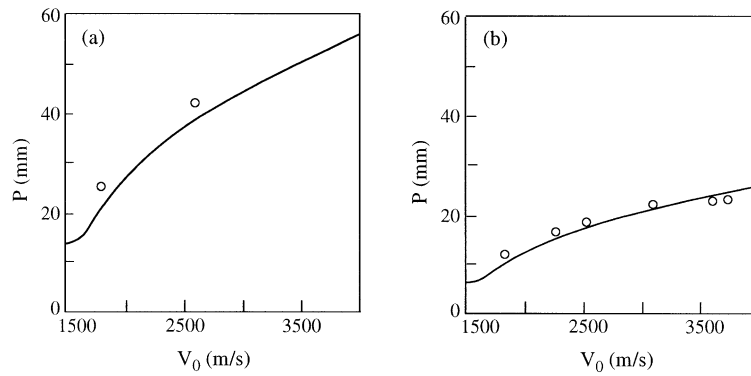


Fig. 4. Penetration depth. Comparison of the computed values with the experimental results (EXP1 and EXP2 in Table 2) for projectiles of different diameters penetrating the same target. (a) EXP1,  $d_0 = 5.4$  mm, (b) EXP2,  $d_0 = 2.5$  mm.

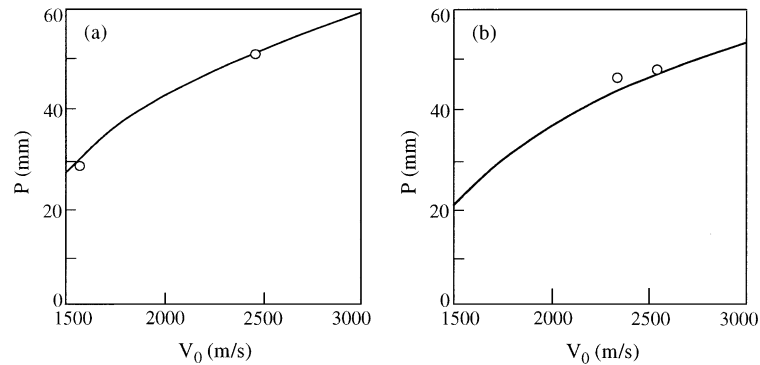


Fig. 5. Penetration depth. Comparison of the computations with the experimental results (EXP3 and EXP4 in Table 2) for the same projectile penetrating targets with different yield stresses. (a) EXP3,  $Y_T = 430$  MPa, (b) EXP4,  $Y_T = 590$  MPa.

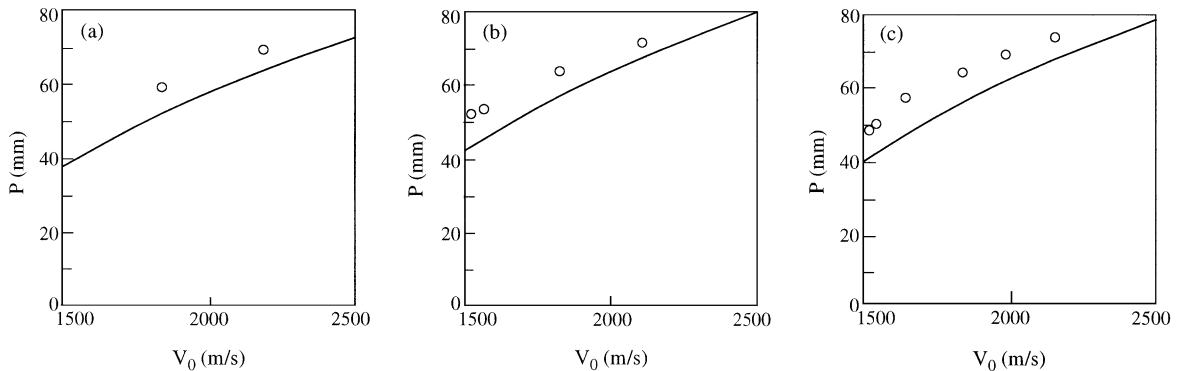


Fig. 6. Penetration depth. Comparison of the computations with the experimental results (EXP5, EXP6, and EXP7 in Table 2) for the projectiles made of different materials penetrating the same target. (a) EXP5,  $\rho_p = 15,500$  kg/m<sup>3</sup>,  $Y_p = 820$  MPa; (b) EXP6,  $\rho_p = 17,300$  kg/m<sup>3</sup>,  $Y_p = 950$  MPa; (c) EXP7,  $\rho_p = 17,000$  kg/m<sup>3</sup>,  $Y_p = 1015$  MPa.

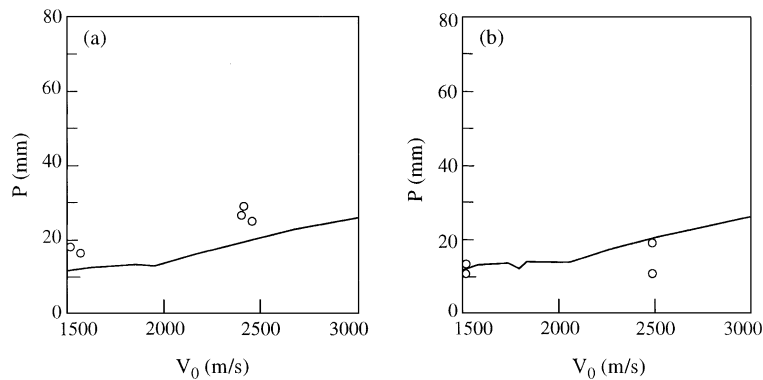


Fig. 7. Penetration depth. Comparison of the computations with the experimental results (EXP8 and EXP9 in Table 2) for the same projectile penetrating targets with different yield stresses and densities. (a) EXP8,  $Y_T = 1263$  MPa,  $\rho_T = 7850$  kg/m<sup>3</sup>; (b) EXP8,  $Y_T = 1448$  MPa,  $\rho_T = 7850$  kg/m<sup>3</sup>.

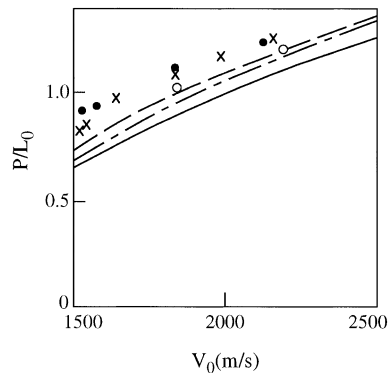


Fig. 8. Normalized data for the penetration depth. The theoretical results are shown by curves and the experimental data are shown by symbols. EXP5: solid line and open circles; EXP6: dashed line and filled circles; EXP7: dashed–dotted line and crosses.

The theoretical curves in Fig. 7 exhibit small kinks between  $V_0 = 1500$  and  $2000$  m/s. As mentioned earlier, the calculation is terminated when either  $U$  or  $L$  vanishes, or Mode PE becomes kinematically inadmissible. Therefore, these kinks at lower impact velocities are mainly attributed to the non-monotonic manner in which these conditions can terminate the calculation. However, in spite of this problem, the results of the present model are in good agreement with experimental data.

Results for the penetration depth in EXP5, EXP6 and EXP7 are combined in Fig. 8 in the same normalized form used in [7,21] to present data for comparison with the usual S-curve. From Fig. 8 it can be concluded that the theoretical curves have about the same spread as the experimental data (which are located a bit above the theoretical predictions). These curves are similar to the middle sections of the S-curves presented in [7,21]. As previously mentioned, the present model does not

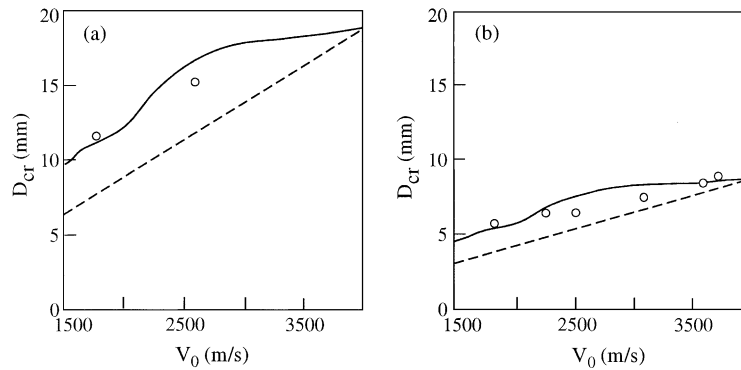


Fig. 9. Crater diameter. Comparison of the computations (solid lines) with the experimental results (EXP1 and EXP2 in Table 2) (symbols), as well as with the asymptotic result (3.48) (dashed lines) for projectiles with different initial diameters penetrating the same target. (a) EXP1,  $d_0 = 5.4$  mm, (b) EXP2,  $d_0 = 2.5$  mm.

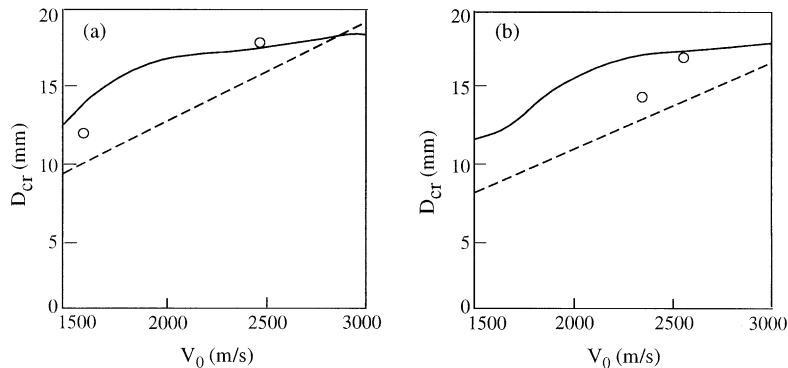


Fig. 10. Crater diameter. Comparison of the computations (solid lines) with the experimental results (symbols), as well as with the asymptotic result (3.48) (dashed lines) for the same projectile penetrating targets with different yield strengths and  $d_0 = 5.4$  mm. (a) EXP3,  $Y_T = 430$  MPa, (b) EXP4,  $Y_T = 590$  MPa.

apply for impact velocities below about 1500 m/s. Moreover, no calculations have been made for impact velocities above about 3500 m/s where the S-curve saturates. However, the theoretical result (3.32) indicates that saturation of the penetration depth follows from the present model for very high impact velocities.

Figs. 9–12 compare the computations of the crater diameter  $D_{cr} = 2R_{cr}$  (solid lines) with the asymptotic result (3.39) (dashed lines) and the experimental results (symbols). The parameters of the penetration process are the same as those in Figs. 4–7. The value of the crater diameter [calculated via Eq. (3.30)] for Mode PE changes with time. Consequently, the residual crater diameter  $D_{cr}$  is taken to be the maximum value of  $2R_{cr}$  obtained during the penetration process and this value is shown in the figures.

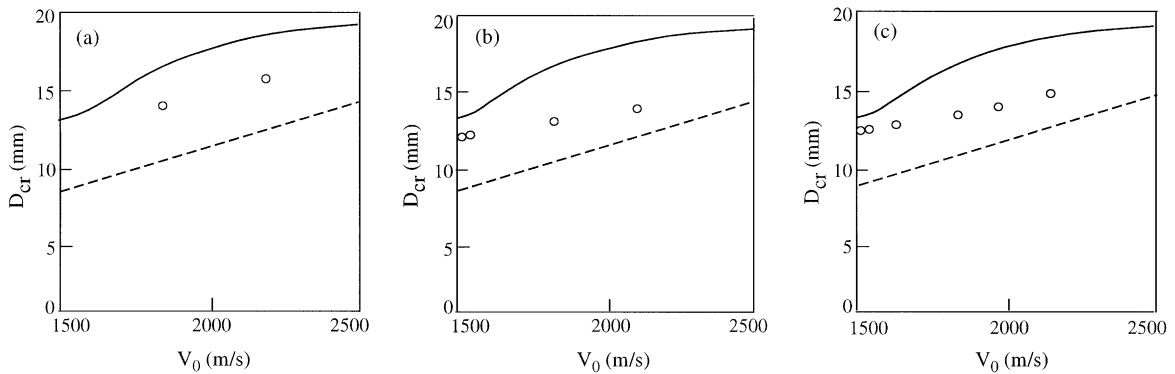


Fig. 11. Crater diameter. Comparison of the computations (solid lines) with the experimental results (symbols), as well as with the asymptotic result (3.48) (dashed lines) for projectiles made from different materials penetrating the same target with  $d_0 = 5.8$  mm. (a) EXP5,  $\rho_p = 15,500$  kg/m<sup>3</sup>,  $Y_p = 820$  MPa; (b) EXP6,  $\rho_p = 17,300$  kg/m<sup>3</sup>,  $Y_p = 950$  MPa; (c) EXP7,  $\rho_p = 17,000$  kg/m<sup>3</sup>,  $Y_p = 1015$  MPa.

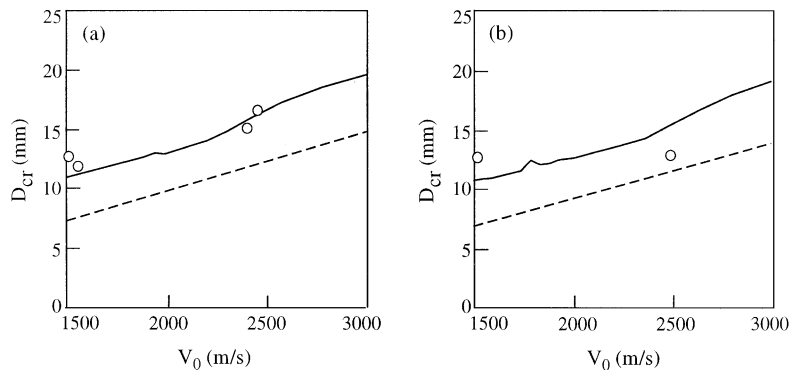


Fig. 12. Crater diameter. Comparison of the computations (solid lines) with the experimental results (symbols), as well as with the asymptotic result (3.48) (dashed lines) for the same projectile penetrating targets with different yield stresses and densities. (a) EXP8,  $Y_T = 1263$  MPa,  $\rho_T = 7850$  kg/m<sup>3</sup>; (b) EXP9,  $Y_T = 1448$  MPa,  $\rho_T = 7850$  kg/m<sup>3</sup>.

## 6. Conclusions

The model developed in the present paper describes penetration of an eroding projectile into an elastic–plastic target. The solution does not use any adjustable parameters or functions and it involves only the geometrical and material data known for the experiments taken from the literature which have been used for comparisons.

The model is capable of predicting the penetration depth, the crater diameter and the residual length and mass of the penetrating projectile. When the yield stress of the projectile  $Y_p$  does not exceed the yield stress  $Y_T$  of the target, the agreement between the theoretical predictions and the experimental data is good. In particular, the agreement between theory and experiment improves as the impact velocity increases and the projectile erosion Mode PE dominates the penetration



process. However, the present model cannot be applied to the cases when  $Y_P \gg Y_T$  or when the density  $\rho_P$  of the projectile is much greater than the density  $\rho_T$  of the target ( $\rho_P \gg \rho_T$ ). A model for these cases is beyond the scope of the present work and is worthy of future research.

The present model has been shown to reduce to the well-known form of the hydrodynamic theory of shaped-charge jets. However, as was known, the crater diameter cannot be determined for very high impact velocities unless the yield stress in the target is included in the analysis. Here, a simplified asymptotic formula for the crater radius has been derived which includes the effect of the target's yield stress. This formula predicts values of the crater diameter which compare well with experimental data for very high impact velocities.

## Acknowledgements

I.V. Roisman was partially supported by Alexander von Humboldt Foundation.

## References

- [1] Birkhoff G, Macdougall DF, Pugh EM, Taylor GI. Explosives with lined cavities. *J Appl Phys* 1948;19:563–82.
- [2] Sagomonyan AYa. Penetration. Moscow: Moscow University Press, 1974 [in Russian].
- [3] Frankel I, Weihs D. Hydrodynamic theory of glancing impact. *J Fluid Mech* 1990;216:213–29.
- [4] Alekseevskii VP. Penetration of a rod into a target at high velocity. *Combust Explos Shock Waves* 1966;2:63–6.
- [5] Tate A. A theory for the deceleration of long rods after impact. *J Mech Phys Solids* 1967;15:387–99.
- [6] Tate A. Further results in the theory of long rod penetration. *J Mech Phys Solids* 1969;17:141–50.
- [7] Walker JD, Anderson Jr CE. A time-dependent model for long-rod penetration. *Int J Impact Engng* 1994;16:19–48.
- [8] Ravid M, Bodner SR. Dynamic perforation of viscoplastic plates by rigid projectiles. *Int J Engng Sci* 1983;21:577–91.
- [9] Ravid M, Bodner SR, Holzman I. Analysis of very high speed impact. *Int J Engng Sci* 1987;25:473–82.
- [10] Ravid M, Bodner SR, Holzman I. A two-dimensional analysis of penetration by an eroding projectile. *Int J Impact Engng* 1994;25:587–603.
- [11] Tate A. A simple hydrodynamic model for the strain field produced in a target by the penetration of a high speed long rod projectile. *Int J Engng Sci* 1978;16:845–58.
- [12] Tate A. Long rod penetration models — Part I. A flow field model for high speed long rod penetration. *Int J Mech Sci* 1986;28:535–48.
- [13] Tate A. Long rod penetration models — Part II. Extensions to the hydrodynamic theory of penetration. *Int J Mech Sci* 1986;28:599–612.
- [14] Roisman IV. Description of projectile penetration with small Deborah number. MSc thesis, Technion, Haifa, 1994.
- [15] Yarin AL, Rubin MB, Roisman IV. Penetration of a rigid projectile into an elastic–plastic target of finite thickness. *Int J Impact Engng* 1995;16:801–31.
- [16] Kochin NE, Kibel IA, Roze NV. Theoretical hydrodynamics. New York: Interscience Pub, 1964.
- [17] Batchelor GK. An introduction to fluid mechanics. Cambridge: Cambridge University Press, 1967.
- [18] Anderson Jr CE, Orphal DL, Franzen RR, Walker JD. On the hydrodynamic approximation for long-rod penetration. *Int J Impact Engng* 1999;22:23–43.
- [19] Lavrentyev MA, Shabat BV. Problems of hydrodynamics and their mathematical models. Moscow: Nauka, 1973 [in Russian].
- [20] Zukas JA. High velocity impact dynamics. New York: Wiley, 1990.
- [21] Anderson Jr CE, Morris BL, Littlefield DL. A penetration mechanics database. Southwest Research Institute Report 359/001, 1992.